

Interface limited growth of heterogeneously nucleated ice in supercooled water

Razvan A. Nistor,¹ Thomas E. Markland,² and B. J. Berne^{1,*}

¹*Department of Chemistry, Columbia University,
3000 Broadway, MC 3103, New York, NY 10027*

²*Department of Chemistry, Stanford University, 333 Campus Drive, Stanford, California 94305*

Heterogeneous ice growth exhibits a maximum in freezing rate arising from the competition between kinetics and the thermodynamic driving force between the solid and liquid states. Here, we use molecular dynamics simulations to elucidate the atomistic details of this competition, focusing on water properties in the interfacial region along the secondary prismatic direction. The crystal growth velocity is maximized when the efficiency of converting interfacial water molecules to ice, collectively known as the attachment kinetics, is greatest. We find water molecules that contact the intermediate ice layer in concave regions along the atomistically roughened surface are more likely to freeze directly. The increased roughening of the solid surface at large undercoolings consequently plays an important limiting role on the rate of ice growth, as water molecules are unable to integrate into increasingly deeper surface pockets. These results provide insights into the molecular mechanisms for self-assembly of solid phases that are important in many biological and atmospheric processes.

I. INTRODUCTION

Self-assembly of a disordered liquid to an ordered solid is one of the most basic physical processes that occurs in nature.^{1,2} Of these processes, the homogenous and heterogeneous growth of ice from liquid water has attracted considerable attention due to its relevance in atmospheric physics,³⁻⁷ cryobiology,^{8,9} and in the antifreeze and food preservation industries.¹⁰⁻¹³ However, while the thermodynamics of freezing is largely understood,^{14,15} the molecular details of the freezing process are less well established.

Owing to the constantly evolving nature of ice growth, it is difficult to probe the moving solid-liquid interfacial region experimentally at the microscopic level. Measurements have shown the ice-water interface to be on the order of ~ 1 nm wide, or three water layers thick.¹⁶ Experiments observing dendritic ice growth have measured maximum growth rates on the order of 10 cm/s for the fastest growing ice faces (the prismatic and secondary prismatic faces).¹⁷⁻²⁰ The temperature dependence of the growth rates deviate away from simple diffusion-limited theories in the experimentally accessible range.^{17,20} This deviation has led to the suggestion that the growth mechanism of crystals is due to a competition between the collective molecular attachment (freezing) and detachment (melting) processes near the solid surface.²⁰⁻²⁵

Molecular dynamics (MD) simulations have proved a useful tool for probing the microscopic properties of the (moving) solid-liquid interface more directly.²⁶⁻³⁸ These studies have also shown the interfacial region is about three water layers wide, and consists of a slushy mix of ice and liquid features whose dynamical properties are greatly arrested compared to the bulk liquid.^{30,32} Ideally, one would like to establish how the structure, shape, dynamics, and molecular attachment rates at the ice surface change with external conditions, such as temperature. What is lacking is a clear microscopic picture of the underlying molecular mechanics defining the crystal growth

process. If the self-assembly mechanism is a competition between the rates of attachment and detachment at the liquid-solid contact, what microscopic properties at the interface favor molecular retention or loss? Furthermore, what microscopic properties explain why the freezing rate reaches a maximum in the supercooled regime?

Here, we use molecular dynamics simulations to investigate how temperature affects the attachment kinetics of water to the secondary prismatic face of ice I_h . We find the temperature dependence of the ice growth rate reaches a maximum when the microscopic efficiency of converting interfacial water to ice is maximum. This efficiency is limited at higher temperatures due to repeated melting and surface migration³⁹ events across the interfacial regions. At lower temperatures, the interplay between the roughening of the ice surface and increased tetrahedrality of the liquid⁴⁰ play important limiting roles. We find molecules which make contact with the intermediate ice layer in concave regions are more likely to freeze directly. Molecules that make contact with regions of higher curvature tend to escape back into the liquid. Consequently, water molecules are unable to rearrange and fit into increasingly deeper surface pockets at very low temperatures. Our results highlight the important role played by interfacial water properties in determining the rate of heterogeneous ice growth at increasingly larger undercoolings.

II. SIMULATIONS DETAILS

Molecular dynamics simulations of the TIP4P/2005 water model⁴¹ were performed using the GROMACS⁴² package on the ice-liquid system shown in Fig. 1a under isobaric-isothermal conditions. Periodic boundary conditions were employed with the long range electrostatics treated using Ewald summation. The pressure was kept at 1 bar using an anisotropic Parrinello-Rahman⁴³ barostat with a time constants of 10 ps. Constant tempera-

ture conditions were imposed using a Langevin thermostat with a time constant of 4.0 ps. Thermostat couplings of 1.0 and 10.0 ps were observed to not affect freezing rates within the statistical error.

The initial ice structure was prepared according to the Bernal-Fowler rules,⁴⁴ and brought in contact with an amorphous water configuration approximately three times the thickness of the ice region. The resulting configuration consisted of a sheet of ice (S) and bulk liquid (L) separated by two ice-liquid interfacial regions (I₁, I₂) shown schematically by the vertical lines in Fig. 1a. Ice growth was monitored perpendicular to the interface along the L_x direction. Ten different trajectories were performed at each of the supercooled temperatures investigated in this study: 220, 230, 235, 240, 242, 245, and 247 K. The simulation cell contained 2696 water molecules. Larger simulations performed with 24,264 water molecules were found to yield similar results for all properties reported.

Water intermolecular interactions were modeled using the fully-atomistic TIP4P/2005 potential. This model was chosen since it has been shown to accurately reproduce the high density phase diagram of water and ice.⁴¹ The melting temperature of the model is 250 K, which is considerably more accurate than the majority of simple point charge water potentials.⁴⁵ Freezing rates obtained with the model are also close to experimentally observed values.³³

Data was only gathered until each trajectory was 60% frozen. This ensured that the close proximity of the two interfacial regions in the simulations cell did not affect the analysis at longer times.

III. INTERFACE IDENTIFICATION

We developed a robust scheme for classifying the evolving ice, liquid, and interfacial regions throughout the freezing process. This classification was accomplished by employing a suitable order parameter to distinguish between local ice- and liquid-like structure, and then using profile functions of this order parameter to identify the instantaneous interface as described below.

A. Instantaneous molecule classification

We used a local tetrahedral order parameter to classify whether the local structure about a water molecule was ice- or liquid-like,⁴⁶

$$S_\theta = \frac{3}{32} \sum_{j=1}^3 \sum_{k=j+1}^4 \left(\cos \theta_{jk} + \frac{1}{3} \right)^2 \quad (1)$$

where the summations extended over all hydrogen bond angles θ_{jk} defined by the nearest four neighboring oxygen atoms around a given molecule. To enhance our ability to distinguish between ice- and liquid-like distributions

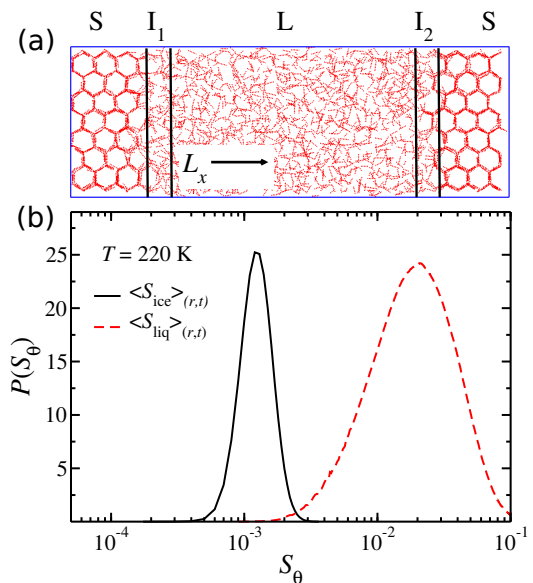


FIG. 1: (a) Initial configuration used in the simulations with schematic outlines of the two interfacial regions (I₁, I₂) separating the solid (S) and liquid (L) phases. Ice grows along the L_x -direction. (b) Tetrahedral order parameter distributions where angle brackets $\langle S \rangle_{(r,t)}$ denote both spatial averaging over several configurations of the trajectory, as well as time-based (exponential) smoothing of the resultant instantaneous order parameters for each molecule in separate bulk ice and liquid simulations. Overlap between ice and liquid distributions is significantly reduced using this scheme. The ice distribution is normalized by 1/45 to make the scale more tractable.

(which can overlap up to 20% at low temperatures), we used a combination of position averaging and exponential time smoothing of the trajectories as described in Appendix A. A water molecule was labeled as ice-like when its resultant order parameter $\langle S_\theta \rangle_t$ was less than a carefully selected threshold criteria S_{tol} . Using the smoothing procedure, near perfect separation between ice and liquid configurations can be obtained with less than 4% overlap between bulk ice and bulk liquid distributions at 220 K, as shown in Fig. 1b. The critical threshold value were chosen to be $S_{tol} = 0.002$ for 220 K, and $S_{tol} = 0.005$ for all other temperatures. At 300 K, no water molecules were misclassified as ice-like in simulations of the bulk liquid. All other observables were calculated from the raw unaveraged trajectories.

B. Instantaneous interface classification

The instantaneous positions of the interfacial regions were identified from profile functions of the tetrahedral order parameter $\langle S_\theta \rangle_t$ projected along the direction of ice growth. This approach is similar to methods used in previous studies to define the extent of the interfacial

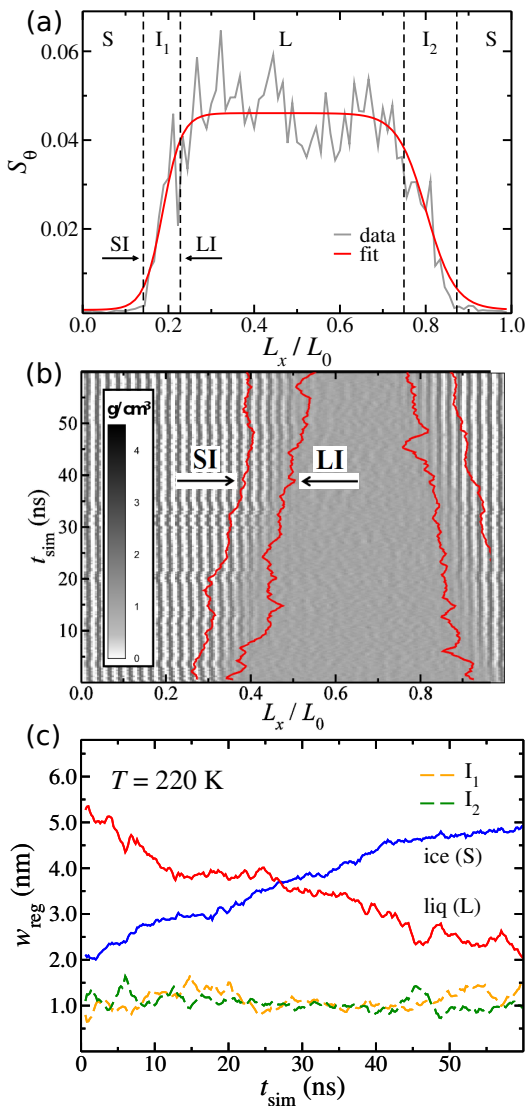


FIG. 2: (a) Tetrahedral order parameter binned along direction of ice growth and resultant profile function used to identify the solid-interface (SI) and liquid-interface (LI) dividing surfaces. (b) Contour map of the density profile evolving during a typical trajectory with the solid lines giving the instantaneous interfacial boundaries (SI and LI) for each interfacial region. (c) Average resultant thicknesses of the ice, liquid, and the widths w_{reg} of the interfacial regions (I_1 , I_2).

region.^{26,30,47} Here, we track two interface boundaries as shown in Fig. 2a: the solid-interface (SI) and the liquid-interface (LI). These dividing surfaces (dashed vertical lines in the figure) were identified using the procedure described in Appendix B.

Fig. 2b shows the projected density along the scaled simulation box for a typical trajectory at 220 K obtained using this scheme. From these boundary lines, the widths of the interfacial regions (I_1 , I_2), and the thicknesses of the ice (S) and liquid (L) regions can be monitored as freezing occurs, as shown in Fig. 2c. Importantly, the in-

terfacial widths remain roughly constant throughout the simulation, and are on the order of ~ 1 nm, or approximately three water layers, consistent with experimental measurements¹⁶ and other MD studies.^{30,34,38,47}

Since ice growth does not proceed on a layer-by-layer basis along the prismatic directions,^{28,32,35} we modeled the rough SI and LI surfaces by dividing the cross-sectional area of the simulation box into a 2D array of fibers extending the entire length of the system along the direction of ice growth. We used 4×5 and 3×3 arrays for this discretization, such that each square fiber was defined by a feature size of $d_f = 0.6$ nm sides. The envelope functions, and subsequently the positions of the SI and LI boundaries, were formed separately in each fiber.

IV. RESULTS AND DISCUSSION

A. Growth rate maximum

The measured ice growth rates R_G along the secondary prismatic direction for different temperatures is shown in Fig. 3a. The growth rate profile reaches a maximum of 9.6 ± 0.5 cm/s at 240 K ($\Delta T_M = -10$ K), in good agreement with previous results using this water model.³⁷ Experimental studies of the growth of ice dendrites report growth velocities of 10-12 cm/s for the fastest growing ice faces at temperatures $\Delta T_M = -18$ K below the melting point.^{17,48}

The maximum in the growth rate in Fig. 3a is characteristic of a crossover from thermodynamically-driven to kinetic-limited crystal growth.^{1,33,40} In the standard picture of freezing,¹⁵ the rate of crystal growth is driven by the chemical potential difference between the solid and liquid phases. As ice becomes thermodynamically more favorable in Fig. 3a, the growth rate increases by a factor of ~ 2 as the temperature is lowered from 247 to 240 K. As the temperature is lowered beyond this point, however, the growth rate decreases. This decrease is described as arising from kinetic barriers governing the attachment of water molecules to the ice surface, which become rate limiting below 240 K.^{1,33}

To assess the efficiency with which water molecules in the interfacial regions are incorporated into the ice phase at the varying temperatures, we consider the interfacial retention probability, α ,

$$\alpha = \frac{\Phi_F - \Phi_R}{\Phi_I}, \quad (2)$$

where Φ_F is the flux (number of molecules per nm^2 per ns) of water molecules that enter the interfacial region from the liquid and freeze, Φ_R is the flux of these frozen molecules that later detach from the solid phase and return to the liquid, and Φ_I is the total flux of molecules that cross into the interfacial region from the liquid and either freeze or escape. Written in this way, α is the percentage of water molecules that freeze relative to the total number of water molecules that cross into the interfacial

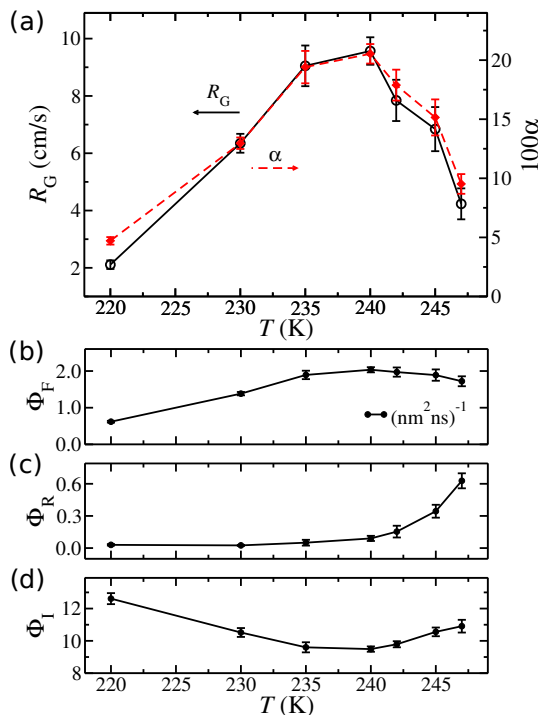


FIG. 3: (a) Average crystal growth velocities R_G (solid line) and retention probabilities α as defined in the text (dashed line) for the secondary prismatic face of ice I_h averaged over all trajectories for each temperature. (b) The flux Φ_F of molecules that freeze. (c) The flux Φ_R of molecules that freeze but later detach from the solid phase and return to the liquid. (d) The total flux Φ_I of molecules that cross into the interfacial region from the liquid.

regions (I_1 and I_2) during the simulation. The temperature dependence of the retention probability (Fig. 3a) follows the same trend observed in the growth rate profile, exhibiting a maximum at 240 K. The retention probability is lowest at the temperature extrema 220 and 247 K. The individual contributions to the retention probability in Figs. 3b-d allow the origins of the freezing inefficiency at low and high temperatures to be assessed.

As can be seen from Fig. 3b, the flux of molecules that freeze Φ_F is almost constant between 247 K to 240 K, but drops by a factor of ~ 4 as the temperature falls from 240 to 220 K (a similar change in freezing rate as observed in Fig. 3a). Conversely, the flux Φ_R of molecules that freeze and later detach from the ice surface increases sharply as the temperature rises as shown in Fig. 3c, by a factor of ~ 10 from 220 to 247 K, where the ice and liquid phases are almost at the same chemical potential. Interestingly, the total flux of molecules into the interfacial region Φ_I , Fig. 3d, shows slightly non monotonic behavior with temperature, though the the maximum at 220 K is only a factor of ~ 1.2 greater than the minimum at 240 K.

Although the system has similarly low retention prob-

abilities and ice growth rates at 220 K and 247 K, the reasons for the limited growth velocities are quite different. At low temperature, the growth rate is limited by a sharp decrease in the number of direct freezing events due to an inability to convert interfacial water molecules into ice before these molecules escape back to the liquid. At high temperatures, the growth rate is limited due to increased flux across the liquid-interface, and the ability of ice molecules to detach from the ice surface and escape back into the liquid once frozen. In the following sections, we analyze how the microscopic dynamics and interface topology contribute to these observations.

B. Effects of interface topology

It is constructive to analyze the collective freezing and melting events at the solid-interface (SI) guided by a simple model. As discussed in Sec. III B, we approximate the roughening of the interfacial dividing surfaces by fitting envelope functions of $\langle S_\theta \rangle_t$ in a series of discretized rectangular fibers extending the length of the simulation box. If the fluctuating position of the solid-interface in each fiber is treated as a biased random walker, where a step forward represents a freezing event, and a step backward represents a melting event, and where the random walk is biased by the degree of undercooling, then ensemble averages over the continuous walks of all the fibers will satisfy,⁴⁹

$$\langle \delta x(\tau) \rangle = \langle x_i(t_0 + \tau) - x_i(t_0) \rangle = (k_f - k_b) a \tau \quad (3)$$

and

$$\langle \delta x^2(\tau) \rangle = \langle \delta x(\tau)^2 \rangle - \langle \delta x(\tau) \rangle^2 = (k_f + k_b) a^2 \tau \quad (4)$$

where $x_i(\tau)$ is the position of the i 'th cell or fiber at time τ , k_f and k_b are the forward (freezing) and backward (melting) rate constants, and a is the average measured step size. Eqn. 3 gives the growth rate (or velocity) as $R_G = (k_f - k_b)a$. Eqn. 4 is a measure of the spread of the random walker trajectories. Using these relations, the forward and backward rate constants can be extracted for each temperature.

Fig. 4a shows the forward and backward rate constants for the two system sizes using a feature size of $d_f = 0.6$ nm for the square fibers defining the discretized random walkers. We have separately verified that the trends are qualitatively reproduced using: (1) Thicker fibers up to $d_f = 1.0$ nm, (2) using interfacial profile functions constructed from the total density ρ ,³⁰ and (3) using trajectories generated using the standard TIP4P water model⁵⁰ (at relative undercoolings).

The forward (freezing) rate constants show a relatively weak dependence as the temperature is lowered below the melting point, increasing by a factor of ~ 1.1 from 247 K to a maximum at 240 K. As the temperature is lowered beyond this point, the forward rate decreases by a factor ~ 1.5 at 220 K. This decrease is indicative of

arrested dynamical timescales limiting the freeze rate at low temperatures as in Fig. 3b.

The backward rate constants (representing molecular detachment events at the solid-interface) show a stronger nonmonotonic temperature dependence. The rates decrease by a factor of ~ 1.5 from 247 K to the minimum at 240 K, and increase by the same factor upon further cooling to 220 K. In other words, the backward rate is highest at the coldest and highest temperature studied. A similar trend was observed for the flux Φ_I into the interfacial region in Fig. 3d. Since the growth rate is a competition between forward and backward processes, i.e. $R_G = (k_f - k_b)a$, the lower growth kinetics is a result of the inability of water molecules to be incorporated in the ice phase at low temperatures, or to remain incorporated in the ice phase at high temperatures.

The microscopic features of the interfacial regions are intricately linked to nonmonotonic temperature dependence of the forward and backwards processes at increasingly lower temperatures. Notably, the structural characteristics of the solid-liquid interface scale differently than in solid-vapor systems, since dangling bonds at the interface can be passivated by the liquid. Fig. 4b shows the root-mean-squared (RMS) deviation of the discretized fibers used to define the instantaneously roughened solid-interface for all temperatures. This shows that the dividing surface becomes rougher as the temperature is lowered, consistent with previous simulations,³⁴ but opposite to what is observed at the ice-vapor interface.^{14,51} The RMS deviation is slightly larger than 0.2 nm at the coldest temperatures, corresponding approximately to an extra ice layer, or half a hexagon as viewed from the basal direction. The larger systems show higher RMS deviations at higher temperatures, which is a notable finite-size effect.

Small systems in particular can lead to overestimated growth kinetics.³³ To understand how this arises, Fig. 4c shows the roughness correlation length ξ extracted from the height-difference spatial correlation function of the large systems,^{52,53}

$$C_h(\Delta\mathbf{R}) = \langle |h(\mathbf{r}) - h(\mathbf{r}')|^2 \rangle, \quad (5)$$

where $h(\mathbf{r})$ is the height of the discretized fiber (in this case, its extent along the x -direction) at position \mathbf{r} along the cross-sectional area of the roughened surface, and $\Delta\mathbf{R} = \mathbf{r} - \mathbf{r}'$. The roughness correlation length was extracted by fitting the function $C_h(\Delta\mathbf{R})$ to the form,⁵³

$$C_h(\Delta\mathbf{R}) = 2\sigma^2 \left\{ 1 - \exp \left[-(\Delta\mathbf{R}/\xi)^{(2P)} \right] \right\}, \quad (6)$$

where σ is the standard deviation in heights, ξ is the correlation length, and P is a roughness exponent, typically between 0.5 and 0.6 for the large systems. The temperature dependence of ξ can be fitted to the Kosterlitz-Thouless scaling relation (dashed line), which increases exponentially and diverges at the roughening transition temperature near the melting point.⁵⁴ At 247 K, the roughness correlation length is nearly 1.6 nm, almost half

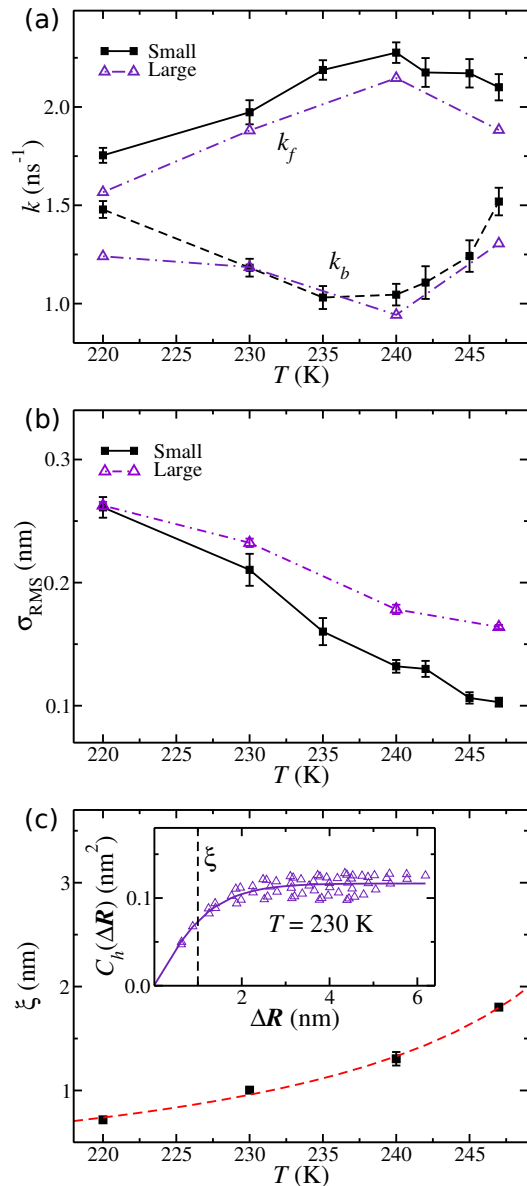


FIG. 4: (a) Forward (k_f) and backward (k_b) rate constants representing freezing and melting processes of the solid-interface for the two different sized systems. (b) The root-mean-squared deviation of the discretized roughened ice surface σ_{RMS} . (c) Spatial correlation lengths ξ for the large systems extracted by fitting the height-difference correlation function as shown in the inset.

the size of the large system simulation cell. These data indicate that finite size effects will become prevalent if long-wavelength capillary waves driving the roughening transition are damped out due to small simulation cells. Higher observed growth rates in sufficiently small systems could result due to the appearance of defected surface motifs that aid molecular rearrangement near the solid surface.^{52,55}

The increase in the roughness correlation length with temperature in Fig. 4c shows structural features are more correlated at higher temperatures. Consequently, the solid-interface appears smoother, with a smaller RMS deviation in the height profiles of the discretized fibers. At lower temperatures, structural correlations occur over shorter lengthscales, and the ice surface becomes rougher.

To gain insight into which properties of the roughened interface inhibit molecular retention at low temperatures, we track where incoming molecules contact the intermediate ice layer (IIL), which is typically composed of a few roughened water layers above the ice boundary as described in Appendix A. We divide the flux of these incoming molecules into molecules that freeze, and molecules that escape back to the liquid without being incorporated in the solid phase. We measure the average distance s of a water molecule to this IIL, and additionally, the curvature H of the roughened surface at the contact point. Contact is defined by the formation of hydrogen bonds between the incoming water molecule and molecules that are part of the IIL. The mean curvature at each point of the atomistically rough intermediate ice surface was calculated from the average of the principal curvatures, $H = \frac{1}{2}(\kappa_1 + \kappa_2)$, where κ_1 and κ_2 are the eigenvalues of the shape operator at the given point on the surface.

As an example, Fig. 5a shows the curvature distributions for the freezing and escaping populations averaged over all trajectories at 230 K. Molecules that directly freeze tend to dock in concave valleys, or regions of negative (or near zero) mean curvature on the roughened intermediate ice surface. Conversely, molecules that escape back into the liquid tend to bind to peaks, or regions of high mean curvature farther away from the solid interface. Particles subsequently have a greater propensity to escape from convex surfaces than from concave surfaces of ice, as seems to be the case for liquid-vapor interfaces as well (see Refs.[52,56]).

Fig. 5b measures the degree of overlap between the freeze and escape distributions for both observables, quantified by taking differences in the mean values: $\Delta H = \langle H_{\text{escape}} \rangle - \langle H_{\text{freeze}} \rangle$ and $\Delta s = \langle s_{\text{escape}} \rangle - \langle s_{\text{freeze}} \rangle$. The differences in both ΔH and Δs decrease as the temperature approaches the melting point, where the solid surface is much flatter. Analogously, there are fewer peaks and valleys for the smoother interfaces at higher temperatures, and less of a docking preference between freeze and escape populations. At large undercoolings, however, the separation between distributions is larger, indicating that escape events preferentially bind to regions of higher curvature.

To assess how the roughened structural features of the ice surface impacts the growth kinetics, Fig. 5c shows Pearson's statistical correlation coefficient g_{corr} between the instantaneous growth rates R_G and surface roughness σ_{RMS} for the large systems. Instantaneous growth rates were obtained from 2.0 ns moving windows centered at each frame of the trajectories. The coefficient is -1.0 when growth rates are completely anticorrelated

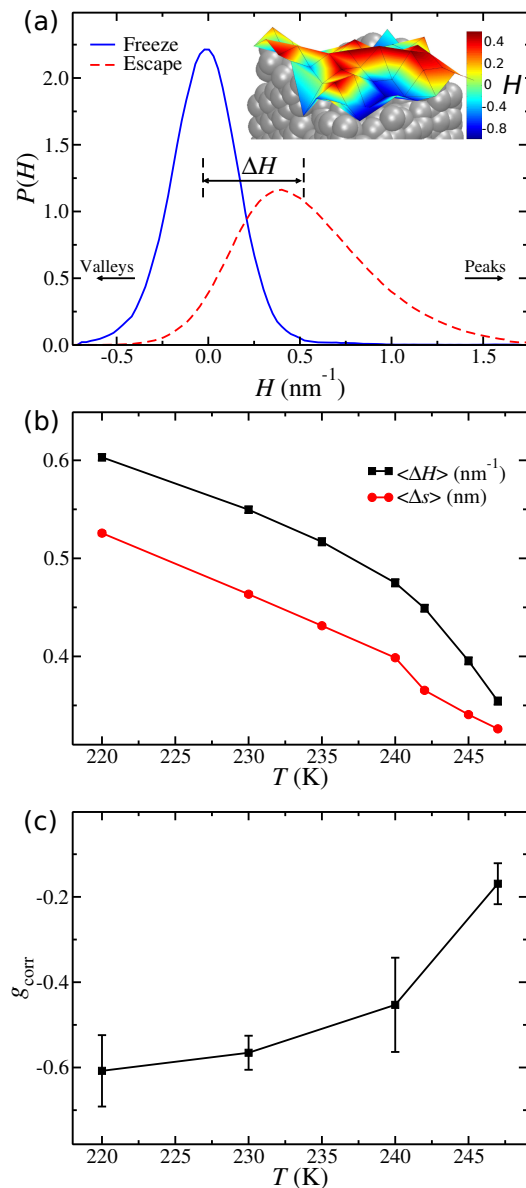


FIG. 5: (a) Mean curvatures $\langle H \rangle$ of freeze, and escape populations at $T = 230$ K. The inset shows a colormap of the resulting curvature values atop an instantaneous configuration of the intermediate ice layer. (b) Differences between freeze and escape distributions for $\langle \Delta s \rangle$ and $\langle \Delta H \rangle$ versus temperature. (c) Statistical correlation g_{corr} between low growth rate and high surface roughness for different temperatures.

with surface roughness. When g_{corr} is 0.0, the two measures are uncorrelated. As can be seen in the figure, g_{corr} approaches 0.0 at high temperatures, and increases to 0.61 ± 0.08 as the temperature is lowered to 220 K. Consequently, *low* growth rates are increasingly associated with *high* surface roughness below the temperature of maximum crystallization.

V. SUMMARY AND CONCLUSIONS

Using molecular dynamics simulations, we have identified structural features of the ice-liquid interface along the secondary prismatic direction that affect crystal growth velocities in the supercooled regime. Near the melting point, the freezing rate is limited by surface depletion events, as molecules detach from the ice and migrate back to the liquid. At much lower temperatures, the topology of the roughened intermediate ice layer plays an important limiting role hindering ice growth. The decrease in the interfacial retention probability at low temperatures is due to the appearance of high-curvature structural motifs. Along with the increased tetrahedrality of the liquid,⁴⁰ these roughened structural profiles limit the crystal growth velocities at larger undercoolings, as the liquid is unable to adjust to the required surface geometry.

At the temperature of maximum crystallization, the efficiency of converting interfacial water to ice is maximized. The rates between competing attachment and detachment reactions in the interfacial region is greatest at this temperature. Notably, molecular detachment rates leading to surface melting are minimized when the crystallization rate is maximized. The liquid is best able to adjust and fill surface pockets at the temperature of maximum growth.

These insights into the molecular scale rate limiting processes for heterogeneous ice nucleation should prove useful in analyzing how other perturbations, such as the presence of solutes, affect the interfacial region and freezing rates. Such an understanding is vital for unraveling the ice growth inhibition mechanisms of antifreeze proteins in biological systems, and for industrial cryogenics applications.

VI. ACKNOWLEDGMENTS

The authors would like to thank Valeria Molinero for her insightful comments on an early version of this manuscript. This research was supported by a grant to BJB from the National Science Foundation (NSF-CHE-0910943). We thank CCNI at RPI and the XSEDE resources at TACC for providing computational facilities to support this project.

Appendix A: Ice-water selectivity

In order to enhance the selectivity between ice- and liquid-like local configurations using the tetrahedral order parameter in Eqn. 1, the atomic positions of the trajectories were first averaged over 5 ps windows to reduce thermal and librational noise in the oxygen atom positions. This time is shorter than the ~ 10 ps characteristic water reorientation time for this water model at 250 K,⁵⁷

which is a higher than any temperature used here and so is much shorter than the characteristic time in which a molecule can interconvert between ice and water in our trajectories. These averaged positions were then used to evaluate the tetrahedral order parameter using Eqn. 1 for each water molecule.

The order parameter history of each water molecule from the position averaged trajectories was then exponentially time-smoothed using, $\langle S_\theta \rangle_t = \alpha S_\theta(t) + (1 - \alpha)\langle S_\theta \rangle_{t-1}$, where $S_\theta(t)$ is the instantaneous order parameter of a given molecule at time t , $\langle S_\theta \rangle_{t-1}$ is the smoothed order parameter of the previous (position-averaged) time step $t - 1$, and α is the smoothing parameter. We found $\alpha \sim 0.3$ gave adequate separation between bulk ice and liquid distributions at low temperatures. This time-based smoothing was used to inhibit instantaneous tetrahedral configurations from contributing to the analysis, which may spontaneously occur even at high temperatures.

Molecules within the interfacial regions whose order parameter $\langle S_\theta \rangle_t$ was greater than the ice threshold criteria S_{toi} , but less than 75% of the liquid value at the given temperature, were labeled as intermediate ice.⁴⁰ A molecule retained its ice, liquid, or intermediate ice label for the duration of the 5 ps position-averaging window. These labels were only used for population analysis.

Appendix B: Interface identification

In order to identify the (moving) positions of the solid- and liquid-interface dividing surfaces, the order parameter $\langle S_\theta \rangle_t$ was binned across the simulation cell as shown in Fig. 2a. The resulting distributions were fitted to profile functions of the form $f(x) = A [\tanh(\frac{x-C}{B}) - \tanh(\frac{x-D}{E})]$, where $\{A, B, C, D, E\}$ were the fit parameters. The roots of the fourth derivative of this function lie close to the positions of the shoulders of the profile and were used here to define the locations of the SI and LI dividing surfaces as shown by the dashed vertical lines in Fig. 2a.

The distributions were accrued over 200 ps time windows. This sampling corresponded to roughly one-tenth the time it took the solid-interface to pass through the next layer of ice in the fastest growing trajectories. The positions of the SI boundaries were aligned with the nearest ice plane at each time step since the lower shoulders of the fitted profile function were not necessarily concomitant with the outermost ice layer. Once the interfacial boundaries were established, molecules could be identified as being in the solid (S), liquid (L), or in one of the two interfacial regions (I_1 , I_2) at any given time in the trajectory. To remove rapid recrossing events across the boundaries, a molecule was required to reside a minimum of 200 ps in a region before it counted towards the population statistics. Molecular configurations and surfaces were rendered using MATLAB and the Visual Molecular Dynamics (VMD) package.^{58,59}

- * Electronic address: bb8@columbia.edu
- ¹ R. J. Kirkpatrick, *Am. Mineral.* **60**, 798 (1975).
 - ² A. C. Levi and M. Kotrla, *J. Phys.: Condens. Matter.* **9**, 299 (1997).
 - ³ V. F. Petrenko and R. W. Whitworth, *Physics of ice* (University Press, Oxford, U. K., 2002).
 - ⁴ T. Koop, B. Luo, A. Tsias, and T. Peter, *Nature* **406**, 611 (2000).
 - ⁵ B. J. Murray, D. A. Knopf, and A. K. Bertram, *Nature* **434**, 202 (2005).
 - ⁶ D. M. Murphy and T. Koop, *Q. J. R. Meteorol. Soc.* **131**, 1539 (2005), ISSN 1477-870X.
 - ⁷ W. Cantrell and A. Heymsfield, *Bull. Amer. Meteor. Soc.* **86**, 795 (2005).
 - ⁸ P. Mazur, *J. Gen. Physiol.* **47**, 347 (1963).
 - ⁹ P. Mazur, **168**, 939 (1970).
 - ¹⁰ M. Griffith and K. V. Ewart, *Biotech. Adv.* **13**, 375 (1995).
 - ¹¹ R. E. Feeney and Y. Yeh, *Trends Food Sci. Technol.* **9**, 102 (1998).
 - ¹² P. A. Carvajal-Rondanelli, S. H. Marshall, and F. Guzman, *J. Sci. Food Agric.* **91**, 2507 (2011).
 - ¹³ M. Hassas-Roudsari and H. D. Goff, *Food Res. Int.* **46**, 425 (2012).
 - ¹⁴ K. G. Libbrecht, *Rep. Prog. Phys.* **68**, 855 (2005).
 - ¹⁵ T. Bartels-Rausch, V. Bergeron, J. H. E. Cartwright, R. Escribano, J. L. Finney, H. Grothe, P. J. Gutiérrez, J. Haapala, W. F. Kuhs, J. B. C. Pettersson, et al., *Rev. Mod. Phys.* **84**, 885 (2012).
 - ¹⁶ D. Beaglehole and P. Wilson, *J. Phys. Chem.* **97**, 11053 (1993).
 - ¹⁷ H. R. Pruppacher, *J. Chem. Phys.* **47**, 1807 (1967).
 - ¹⁸ J. S. Langer, R. F. Sekerka, and T. Fujioka, *J. Crys. Growth* **44**, 414 (1978).
 - ¹⁹ Y. Furukawa and W. Shimada, *J. Crys. Growth* **128**, 238 (1993).
 - ²⁰ A. Shibkov, M. Zheltov, A. Korolev, A. Kazakov, and A. Leonov, *J. Crys. Growth* **285**, 215 (2005).
 - ²¹ H. A. Wilson, *Phil. Mag.* **50**, 238 (1900).
 - ²² J. Frenkel, *Phys. Z. Sowjet Union* **1**, 498 (1932).
 - ²³ A. N. Kolmogorov, *Bull. Acad. Sci. URSS (Cl. Sci. Math. Nat.)* **3**, 355 (1937).
 - ²⁴ W. A. Johnsson and R. F. Mehl, *Trans. Am. Inst. Min. Metall. Eng.* **135**, 416 (1940).
 - ²⁵ M. Avrami, *J. Chem. Phys.* **8**, 212 (1940).
 - ²⁶ O. A. Karim and A. D. J. Haymet, *Chem. Phys. Lett.* **138**, 531 (1987).
 - ²⁷ A. D. J. Karim O. A. Haymet, *J. Chem. Phys.* **89**, 6889 (1988).
 - ²⁸ H. Nada and Y. Furukawa, *Jpn. J. Appl. Phys.* **34**, 583 (1995).
 - ²⁹ L. A. Baéz and P. Clancy, *J. Chem. Phys.* **103**, 9744 (1995).
 - ³⁰ J. A. Hayward and A. D. J. Haymet, *J. Chem. Phys.* **114**, 3713 (2001).
 - ³¹ J. A. Hayward and A. D. J. Haymet, *Phys. Chem. Chem. Phys.* **4**, 3712 (2002).
 - ³² M. A. Carignano, P. Shepson, and I. Szleifer, *Mol. Phys.* **103**, 2957 (2005).
 - ³³ D. Rozmanov and P. G. Kusalik, *Phys. Chem. Chem. Phys.* **13**, 15501 (2011).
 - ³⁴ P. Pirzadeh, E. N. Beaudoin, and P. G. Kusalik, *Crys. Growth Des.* **12**, 124 (2012).
 - ³⁵ M. Seo, E. Jang, K. Kim, S. Choi, and J. S. Kim, *J. Chem. Phys.* **137**, 154503 (2012).
 - ³⁶ D. Rozmanov and P. G. Kusalik, *Phys. Chem. Chem. Phys.* **14**, 13010 (2012).
 - ³⁷ D. Rozmanov and P. G. Kusalik, *J. Chem. Phys.* **137**, 094702 (2012).
 - ³⁸ T. D. Shepherd, M. A. Koc, and V. Molinero, *J. Phys. Chem. C* **116**, 12172 (2012).
 - ³⁹ M. J. Rost, D. A. Quist, and J. W. M. Frenken, *Phys. Rev. Lett.* **91**, 026101 (2003).
 - ⁴⁰ E. B. Moore and V. Molinero, *Nature* **479**, 506 (2011).
 - ⁴¹ J. L. F. Abascal and C. Vega, *J. Chem. Phys.* **123**, 234505 (2005).
 - ⁴² B. Hess, C. Kutzner, D. van der Spoel, and E. Lindahl, *J. Chem. Theory Comput.* **4**, 435 (2008).
 - ⁴³ M. Parrinello and A. Rahman, *J. Appl. Phys.* **52**, 7182 (1981).
 - ⁴⁴ J. D. Bernal and R. H. Fowler, *J. Chem. Phys.* **1**, 515 (1933).
 - ⁴⁵ R. G. Fernández, J. L. F. Abascal, and C. Vega, *J. Chem. Phys.* **124**, 144506 (2006).
 - ⁴⁶ P.-L. Chau and A. J. Hardwick, *Mol. Phys.* **93**, 511 (1998).
 - ⁴⁷ M. S. G. Razul and P. G. Kusalik, *J. Phys. Chem.* **134**, 014710 (2011).
 - ⁴⁸ S. Bauerecker, P. Ulbig, V. Buch, L. Vrbka, and P. Jungwirth, *J. Phys. Chem. C* **112**, 7631 (2008).
 - ⁴⁹ F. Spitzer, *Principles of random walk* (Springer-Verlag, New York, U. S. A., 1976).
 - ⁵⁰ W. L. Jorgensen, J. Chandrasekhar, J. D. Madura, R. W. Impey, and M. L. Klein, *J. Chem. Phys.* **79**, 926 (1983).
 - ⁵¹ J. W. Cahn and J. E. Hilliard, *J. Chem. Phys.* **28**, 258 (1958).
 - ⁵² J. D. Weeks and G. H. Gilmer, in *Advances in chemical physics*, edited by I. Prigogine and S. A. Rice (John Wiley, New York, 1979), vol. 40, pp. 157–228.
 - ⁵³ T. Salditt, T. H. Metzger, C. Brandt, U. Klemradt, and J. Peisl, *Phys. Rev. B* **51**, 5617 (1995).
 - ⁵⁴ J. M. Kosterlitz and D. J. Thouless, *J. Phys. C: Sol. Stat. Phys.* **6**, 1181 (1973).
 - ⁵⁵ J. Q. Broughton and G. H. Gilmer, *J. Chem. Phys.* **79**, 5119 (1983).
 - ⁵⁶ A. P. Willard and D. Chandler, *J. Phys. Chem. B* **114**, 1954 (2010).
 - ⁵⁷ G. Stirnemann and D. Laage, *J. Chem. Phys.* **137** (2012).
 - ⁵⁸ MATLAB, *version 7.0.1 (R14SP1)* (The MathWorks Inc., Natick, Massachusetts, 2005).
 - ⁵⁹ W. Humphrey, A. Dalke, and K. Schulten, *J. Mol. Graph.* **14**, 33 (1996).